Craig A. Steeves
Postdoctoral Scholar

Ming Y. He
Project Scientist

Department of Materials,
University of California, Santa Barbara,
Santa Barbara, CA 93106

Scott D. Kasen
Graduate Student
Department of Materials Science and Engineering,
University of Virginia,
Charlottesville, VA 22904

Lorenzo Valdevit
Assistant Professor
Department of Mechanical and Aerospace Engineering,
University of California, Irvine,
Irvine, CA 92697

Haydn N. G. Wadley
Professor
Department of Materials Science and Engineering,
University of Virginia,
Charlottesville, VA 22904

Anthony G. Evans
Professor
Department of Materials,
University of California, Santa Barbara,
Santa Barbara, CA 93106

Feasibility of Metallic Structural Heat Pipes as Sharp Leading Edges for Hypersonic Vehicles

Hypersonic flight with hydrocarbon-fueled airbreathing propulsion requires sharp leading edges. This generates high temperatures at the leading edge surface, which cannot be sustained by most materials. By integrating a planar heat pipe into the structure of the leading edge, the heat can be conducted to large flat surfaces from which it can be radiated out to the environment, significantly reducing the temperatures at the leading edge and making metals feasible materials. This paper describes a method by which the leading edge thermal boundary conditions can be ascertained from standard hypersonic correlations, and then uses these boundary conditions along with a set of analytical approximations to predict the behavior of a planar leading edge heat pipe. The analytical predictions of the thermostructural performance are verified by finite element calculations. Given the results of the analysis, possible heat pipe fluid systems are assessed, and their applicability to the relevant conditions determined. The results indicate that the niobium alloy Cb-752, with lithium as the working fluid, is a feasible combination for Mach 6–8 flight with a 3 mm leading edge radius. [DOI: 10.1115/1.3086440]

1 Background

For aerodynamic reasons hypersonic vehicles require sharp leading edges, with millimeter scale radius. When the edges are that sharp, the heat flux into the structure is intense. Specifically, at Mach 6–8 (the highest Mach number attainable with hydrocarbon fuels), the fluid stagnation temperature $T_{st} > 1400\,^{\circ}\mathrm{C}$, exceeding the realistic upper use temperature of most materials. Because the tip must remain sharp and have a stable shape, ablative solutions are very challenging. Instead, the heat must be rapidly redistributed through the solid to enable dissipation by radiation from the largest possible area of the vehicle surface. The three primary passive options to obtain such a solution are (i) carbon-fiber-based composites that retain load-bearing capability at $T \to T_{st}$, (ii) ultrahigh temperature ceramics (such as HfB_2) that combine refractoriness $T_M > T_{st}$ with large thermal conductivity at $T \to T_{st}$, and (iii) heat pipes, which enable allowable equilibrium temperatures by providing exceptional effective thermal conductivity, k_{eff}.

This assessment addresses the performance of heat pipes incorporated within metallic leading edge structures during steady-state hypersonic cruise. The preferred configuration has a curved surface fully defined by the thickness t, the leading edge radius R_{le}, and the angle ϕ_0 (which is the complement of the wedge half-angle θ) at which the curved front connects to the flat radiating surface (see Fig. 1). The design length of the radiating surface, L, must be chosen to ensure that the materials remain below their maximum use temperature.

Heat pipes have been pursued previously in the context of leading edges and other high temperature applications [1,2]. The present structural heat pipe differs in the sense that the design not only equilibrates the temperature but also supports transverse and shear loads (Fig. 2). For manufacturing facility and robustness, all-metallic designs are pursued, and their feasibility up to Mach 8 deduced.

Because of the crucial role of radiation, the temperatures induced are a strong function of the emissivity, ϵ, of the radiating surface. While ϵ can be quite low for conventional alloys, the refractory alloys to be explored here can be designed to have larger values by pre-oxidizing to form either alumina or silica. The most well-documented are the nickel alloys used in turbines, which, when used with a bond coat, form a highly adherent, thin layer of α-Al_2O_3 [3] with (at high temperature) $\epsilon \geq 0.9$.

Contributed by the Applied Mechanics Division of ASME for publication in the JOURNAL OF APPLIED MECHANICS. Manuscript received January 25, 2008; final manuscript received May 7, 2008; published online March 13, 2009. Review conducted by Martin Ostoja-Starzewski.

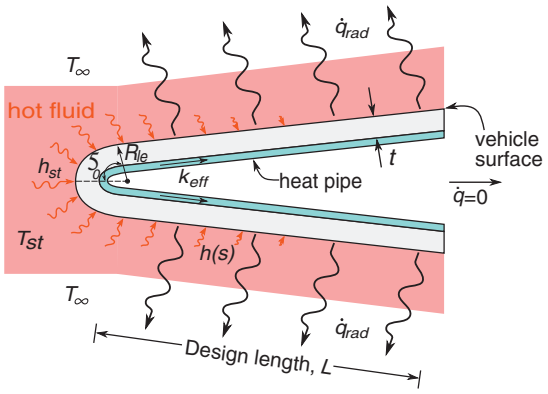

Fig. 1 The local geometry and flow conditions near the leading edge

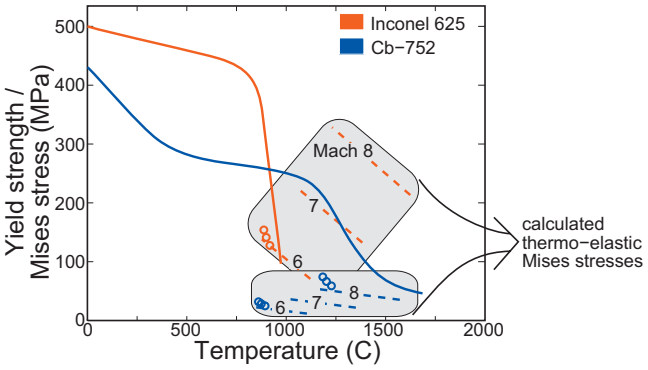

Fig. 3 The temperature dependence of the yield strength for the two refractory alloys, Inconel 625 (red) and Cb-752 (blue), used in the analysis, shown as solid lines. Analytical cross-plots of maximum stress as a function of temperature are presented as dashed lines for Mach 6–8. The corresponding finite element results are plotted as circles.

To address this challenge, this paper is structured as follows: The aerothermodynamic environment that governs the heat flux into the leading edge is characterized using procedures based on the stagnation temperature and heat transfer coefficient. Steady-state temperatures and heat fluxes induced when the heat pipe is functioning are derived using analytic approximations with the fidelity assessed using selected finite element calculations. The designs to be explored are based on nickel (Inconel 625) and niobium (Cb-752) alloys having the properties in Table 1 and temperature-dependent yield strength characteristics presented in Fig. 3. Other refractory alloys, such as those based on molybdenum, tungsten, or rhenium, could be envisaged using the same basic protocol. The differing temperature and stress circumstances that arise during transients before the heat pipe begins to function are examined, as well as the influence of thin oxidation-protective coatings on the metallic surface. The operational requirements on the heat pipe are checked against models of heat pipe behavior to ensure the functionality of the system at the requisite heat flux and physical dimensions.

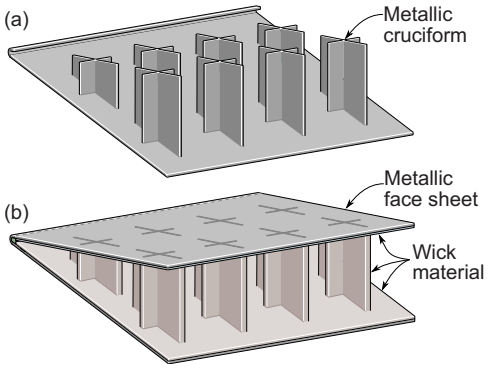

Fig. 2 A structural heat pipe for the leading edge of a hypersonic vehicle showing (*a*) a cutaway view with the metallic wick material removed to show the cruciform structural members, and (*b*) the assembly with both metallic faces and the wick installed

2 The Leading Edge Aerothermodynamic Environment

Stagnation conditions. For hypersonic vehicles powered by scramjet engines with hydrocarbon fuels, the Mach number at cruise ranges between 6 and 8. The relation between Mach number and altitude is determined by requiring that the vehicle flies at a constant dynamic pressure (typically 48 kPa [4]). For each altitude, the freestream temperature T_∞, pressure P_∞, and density ρ_∞ are found in standard atmosphere tables [5], summarized in Table 2.

The total freestream enthalpy H_∞ is related to the temperature and vehicle velocity, u_∞, by

$$H_\infty = c_p T_\infty + u_\infty^2/2 \tag{1}$$

where $c_p = 1.04$ kJ/kg K is the specific heat of quiescent air. The pressure at the stagnation point is obtained by assuming that the kinetic energy of the fluid is converted completely to pressure, and that $P_{st} \gg P_\infty$ [6],

$$P_{st} \approx \rho_\infty u_\infty^2 \tag{2}$$

The stagnation temperature can be found using a Mollier diagram [7], which is implemented in the Hypersonic Airbreathing Propulsion (HAP) software [4]. The results are summarized in Table 2.

Heat flux. Herein is a strategy for determining the aerothermal loading. The premise is that the air close to the surface at the leading edge reaches the full gas stagnation temperature. Heat enters the leading edge at a rate governed by a spatially varying heat transfer coefficient. A heat pipe on the back surface of the leading edge transfers the heat to a flat region, from which the heat is then radiated into low temperature space (Fig. 1). The system is heat balanced, such that the total heat entering the vehicle through convection is equal to that leaving by radiation. The following describes how to calculate the heat transfer coefficient and heat flux.

Table 1 Relevant material properties of nickel-based superalloy Inconel 625 and niobium alloy Cb-752. The temperature-dependent material properties are taken at 800°C.

	Density ρ (kg/m^3)	Specific heat c_p (J/kg K)	Thermal conductivity k (W/m K) (at 800°C)	Thermal expansion α (ppm/K) (at 800°C)	Young's modulus E (GPa) (at 800°C)
Inconel 625	8440	525	21	15	155
Cb-752	9030	281	48	7.4	110

Table 2 Atmospheric properties and calculated stagnation conditions for flight over the range of Mach 6 to 8 with constant dynamic pressure of 48 kPa

Mach No.	Altitude (km)	Temperature T_∞ (K)	Pressure P_∞ (Pa)	Density ρ_∞ (kg/m^3)	Velocity u_∞ (km/s)	Enthalpy H_∞ (MJ/kg)	Stagnation temperature T_{st} (K)
6	26.93	223.5	1900	0.0296	1.80	1.85	1651
7	28.98	225.5	1396	0.0215	2.11	2.46	2122
8	30.76	227.3	1069	0.0160	2.42	3.16	2627

Fay and Riddell [8] used the results of Lees [9] to ascertain correlations for the heat flux at the stagnation point. Sutton and Graves [10] approximated these by

$$\dot{q} = (H_g - H_w)K\sqrt{\frac{P_{st}}{R_{le}}} \tag{3}$$

where H_g is the local fluid enthalpy, H_w is the local wall enthalpy, and K is a heat transfer factor, which is a function of molecular weight, the mass fractions of the constituent gases, and a gas-dependent transport parameter. Sutton and Graves [10] used the results of Svehla [11] to calculate $K=3.6\times10^{-4}$ m^{-1} kg$^{-1/2}$ for air. For the Mach numbers under investigation, $H_g \gg H_w$; consequently, by setting $H_w=0$ and $H_g \approx H_\infty$, Eq. (3) becomes the "cold-wall" heat flux. At the stagnation point,

$$\dot{q}_{cw,st} = H_\infty K\sqrt{\frac{P_{st}}{R_{le}}} \tag{4}$$

The heat transfer coefficient at this location h_{st} can be approximated through

$$h_{st} = \dot{q}_{cw,st}/T_{st} \tag{5}$$

which varies around the curved leading edge as $h(\phi)=h_{st}\cos(\phi)$. Beyond the curved section, the heat transfer coefficient declines as $h(s)\sim s^{-1/2}$, calculated as shown in Fig. 4. The actual vehicle surface is given by the solid line. Equating the heat transfer at the transition from the curved to flat sections, the coefficient along the radiating surface becomes

$$h(s) = h_{st}\cos\phi_0\frac{\sqrt{R_{le}}}{\sqrt{s\tan\theta}} \tag{6}$$

These equations permit calculation of the fluid temperature and local heat transfer coefficient around the leading edge. Implicit in this approach is the assumption that h is unaffected by the surface temperature T_{surf} and, accordingly, can be used to determine the actual heat flux once T_{surf} has been ascertained. The dependence of the stagnation point heat transfer coefficient on the leading edge radius for the Mach numbers of interest is displayed in Fig. 5; it is independent of the material properties of the leading edge.

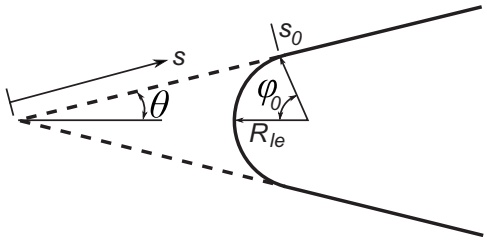

Fig. 4 The assumed geometry for the calculation of the heat transfer coefficient along the flat radiating surface. The actual geometry is depicted with solid lines, while the dashed lines indicate the geometry for a perfectly sharp leading edge.

3 Steady-State Temperatures and Thermal Stresses

3.1 Analytical Estimates. *Isothermal temperature*. When the heat pipe is functioning and the wall is thin, the solid approaches an isothermal temperature, T_{iso}, except very close to the leading edge. Thus, T_{iso} becomes a useful reference temperature as well as the nominal temperature of the working fluid in the heat pipe. Under this thermal condition, the system is heat balanced. The spatial extent of the solid that attains T_{iso} will be addressed later. The heat entering through the curved surface is given by

$$Q_{in}^c = \int_0^{\phi_0} R_{le}h_{st}\cos\phi(T_{st}-T_{iso})\mathrm{d}\phi \equiv R_{le}h_{st}\sin\phi_0(T_{st}-T_{iso}) \tag{7}$$

Through the flat surface the convective heat transfer is given by

$$Q_{in}^f = \int_{s_0}^{s_0+L} h(s)(T_{st}-T_{iso})\mathrm{d}s \equiv \frac{2h_\phi\sqrt{R_{le}}}{\tan\theta}(\sqrt{R_{le}+L\tan\theta}-\sqrt{R_{le}}) \times(T_{st}-T_{iso}) \tag{8}$$

with $h_\phi=h_{st}\cos(\phi_0)$ and s the distance along the radiating surface as sketched in Fig. 4. The heat radiated out through the entire leading edge surface is

$$Q_{out} = \int_0^{L_{tot}} \epsilon\Sigma T_{iso}^4\mathrm{d}s \equiv \epsilon\Sigma L_{tot}T_{iso}^4 \tag{9}$$

where L_{tot} is the total length of the heat pipe ($L_{tot}=R_{le}\phi_0+L$) and $\Sigma=5.67\times10^{-8}$ W/m^2 K^4 is the Stefan–Boltzmann constant. Heat balance requires that $Q_{in}=Q_{out}$, and hence

$$R_{le}h_{st}\sin\phi_0(T_{st}-T_{iso}) + \frac{2h_\phi\sqrt{R_{le}}}{\tan\theta}(\sqrt{R_{le}+L\tan\theta}-\sqrt{R_{le}})(T_{st}-T_{iso}) - \epsilon\Sigma L_{tot}T_{iso}^4 = 0 \tag{10}$$

which can be solved for T_{iso}. The results are plotted in Fig. 6(a), as a function of the length of the radiating surface, for R_{le}

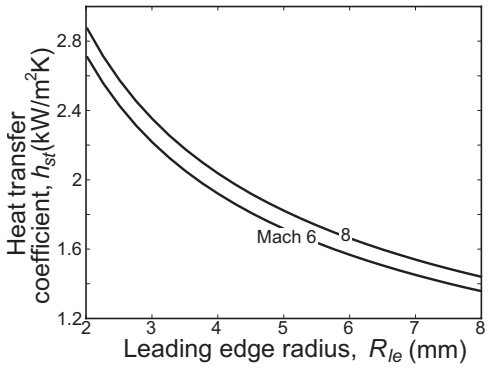

Fig. 5 The stagnation point heat transfer coefficient as a function of the leading edge radius for a range of Mach numbers

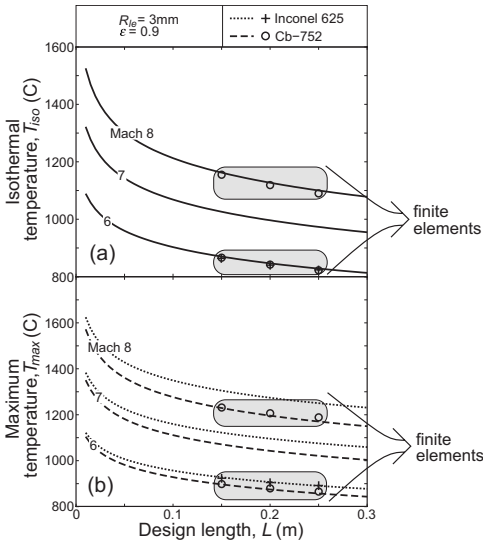

Fig. 6 The leading edge temperatures calculated analytically (lines) over the relevant range of parameters, and by finite elements (circles and crosses) at Mach 6 and 8 for a vehicle with R_{le}=3 mm, ϵ=0.9, and θ=6 deg. (*a*) The isothermal temperature approximation as a function of the length of the radiating surface. Note that the analytical predictions are identical for the two materials, and that the finite element calculations at Mach 6 for Inconel 625 and Cb-752 fall on top of each other. (*b*) The maximum temperature at the stagnation point on the surface of the leading edge for Inconel 625 (dots and crosses) and Cb-752 (dashes and circles).

=3 mm, ϵ=0.9, and θ=6 deg. Note that the isothermal temperature is sensitive to the design length L but independent of the material chosen for the system.

Maximum temperature. The maximum temperature at the stagnation point can be estimated by assessing the heat flux across a small element, length $R_{le}d\phi$ (Fig. 7) by using a one-dimensional calculation for heat flow into a hollow cylinder. Implicit to this estimation is that the heat flux through the wall is much larger than that along the surface (justified below). The general equation for steady-state heat conduction is

$$k\left(\frac{\partial^2 T}{\partial r^2}+\frac{1}{r}\frac{\partial T}{\partial r}\right)=0 \tag{11}$$

with k the thermal conductivity of the material and r the radial distance from the center. The boundary conditions are set by the stagnation temperature and heat transfer coefficient of the gas, as well as by the premise that the internal surface is at temperature

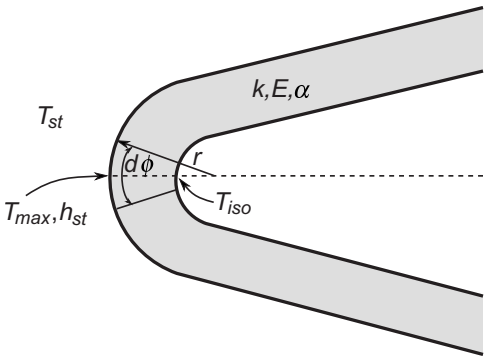

Fig. 7 A sketch of the region along the stagnation line for which the temperatures are solved by a cylindrical finite difference scheme

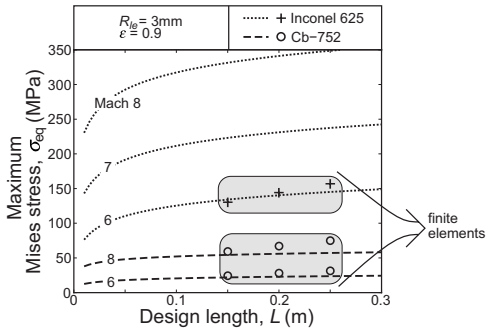

Fig. 8 The maximum thermally induced Mises stress at the exterior surface along the stagnation plane for a vehicle with R_{le}=3 mm, ϵ=0.9, and θ=6 deg. The analytical results are lines, while the finite element results are circles and crosses.

T_{iso}. The solution for the maximum material temperature at the outside surface is

$$T_{max}=\frac{T_{iso}+T_{st}\left(\frac{R_{le}h_{st}}{k}\ln\frac{R_{le}}{R_i}\right)}{1+\left(\frac{R_{le}h_{st}}{k}\ln\frac{R_{le}}{R_i}\right)} \tag{12}$$

where $R_i=R_{le}-t$ is the inner radius of the leading edge. The maximum temperatures T_{max} for R_{le}=3 mm, t=1 mm, and ϵ=0.9, for Inconel 625 (k=21 W/m K) and Cb-752 (k=48 W/m K) at Mach 6–8, are plotted in Fig. 6(*b*) for a range of design lengths. This temperature is a function of the material thermal conductivity with higher conductivity leading to lower T_{max}. The corresponding heat flux through the surface into the heat pipe is

$$\dot{q}=\frac{k(T_{max}-T_{iso})}{R_i\ln\frac{R_{le}}{R_i}} \tag{13}$$

Stresses. Because the structure is metallic, the Mises stress near the leading edge (where the temperature is largest), relative to the yield strength, governs the integrity. To estimate the thermoelastic stress (no yielding), the reference state is taken to be the long straight segment at T_{iso}. The thermal expansion misfit of the tip region, relative to this state, generates a stress. Neglecting bending (justified later), the stress is dominated by the out-of-plane strain misfit and varies through the thickness as

$$\sigma_{eq}(r)=\alpha E(T(r)-T_{iso}) \tag{14}$$

The maximum at the exterior surface is plotted in Fig. 8 over the relevant range of Mach numbers. The maximum increases with larger L because, as the length increases, the total heat radiated away increases, *despite the decreased overall temperature*, requiring a larger thermal gradient at the leading edge to provide the greater heat flux. Hence, as the design length increases, the maximum temperature decreases while the maximum stress increases. Cross-plots of the relation between maximum stress and maximum temperature are shown in Fig. 3 for comparison with the material yield strength at that temperature. For longer design lengths (toward the left side of the graph) and lower Mach numbers, the operational conditions are clearly within the elastic envelope of the materials. However, above Mach 6, the stresses exceed the yield strength of Inconel 625 at the operating temperatures, thereby excluding this alloy from use. Conversely, Cb-752 retains its integrity even up to Mach 8, due to its combination of thermomechanical properties discussed below.

Without a heat pipe. In the absence of a heat pipe, heat is transferred only by longitudinal conduction along the curved region into the radiating surface, resulting in the temperature distributions plotted in Fig. 9 for Mach 7 flight for a Cb-752 leading

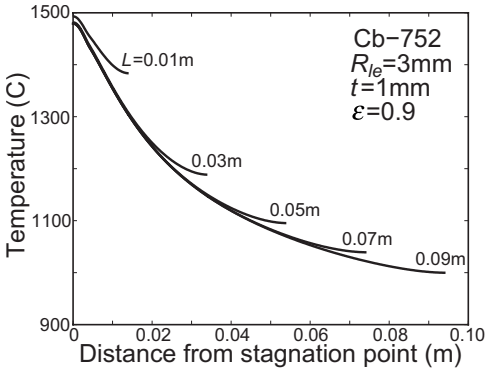

Fig. 9 The behavior of the leading edge in the absence of a heat pipe: The temperature distribution along the length of an Cb-752 (k=48 W/m K) leading edge at Mach 7 for a range of design lengths L, assuming that the material is isothermal through the thickness and that ϵ=0.9, R_{le}=3 mm, and t =1 mm

edge. A steep temperature gradient develops along the length and the maximum temperatures become insensitive to L. Comparison with Fig. 6 demonstrates the importance of having a functioning heat pipe.

3.2 Finite Element Calculations. *Method*. All calculations are conducted using the commercial finite element code ABAQUS. In the analysis, eight-node coupled temperature-displacement generalized plane strain elements are used. Symmetry conditions are imposed on AD in the y-direction and on CF in the x-direction (Fig. 10). The solids are incorporated as an elastic/plastic medium having temperature-dependent yield strength (Fig. 3) with nominal strain hardening.

The external thermal boundary conditions are the same as those described in Sec. 2. Outside the entire surface, the air is assigned the stagnation temperature, with a heat transfer coefficient that varies spatially over ϕ and s. This temperature difference with that computed for the solid surface, T_{surf}, then governs the inward heat flux. Radiation to ambient T_∞ from the surface, at T_{surf}, determines the outward heat flux. ABAQUS simultaneously solves for the net flux and T_{surf}, as well as the Mises stresses and (when yielding occurs) equivalent plastic strains. Conduction through the solid is characterized by a (temperature invariant) thermal conductivity, k. The action of the internal heat pipe is simulated by imposing a thin (1 mm) compliant layer on the inside having exceptional effective thermal conductivity, k_{eff} (Fig. 1). Effective thermal conductivities in excess of 100 times that of solid copper have been reported [12]. A conservative value of k_{hp} =3 kW/m K was used in all simulations. The thermo-elastic properties of Inconel 625 and Cb-752 used in the calculations are those presented in Table 1 and Fig. 3. Results are presented for a

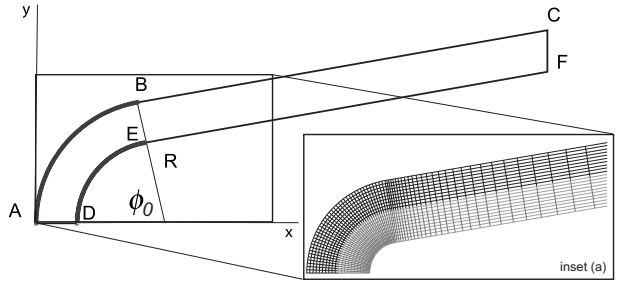

Fig. 10 A typical finite element mesh used in the simulations. The solid metallic component is represented in black, while the heat pipe is in gray.

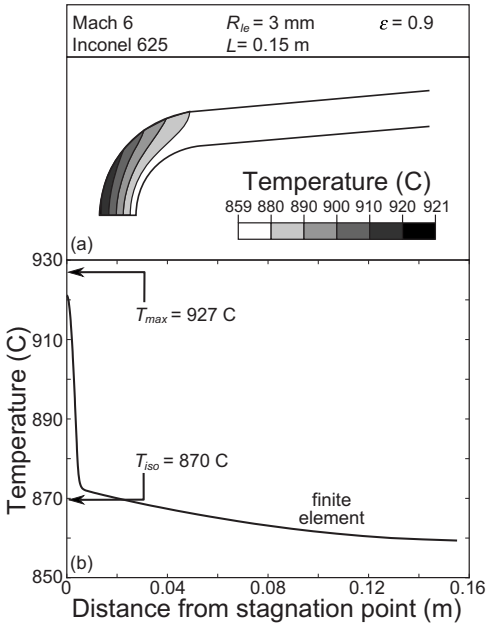

Fig. 11 (*a*) Contours of the temperatures induced in the nickel alloy at Mach 6 when the heat pipe is functioning. (*b*) The temperatures along the external surface with analytic results for T_{iso} and T_{max} for ϵ=0.9 are superimposed.

leading edge with radius R_{le}=3 mm and wedge half-angle θ =6 deg.

Temperatures and heat fluxes. In order to compare with the analytic estimates, the temperatures have been obtained for the nickel alloy at Mach 6 and the niobium alloy at Mach 6 and 8 (as a function of design length). Representative temperature distributions are plotted in Figs. 11 and 12 (for L=0.15 m). The straight sections, as well as the inside of the curved tip, are at essentially uniform temperature, identified with T_{iso}. The outside temperature at the tip is appreciably hotter, with largest value, T_{max}, at the

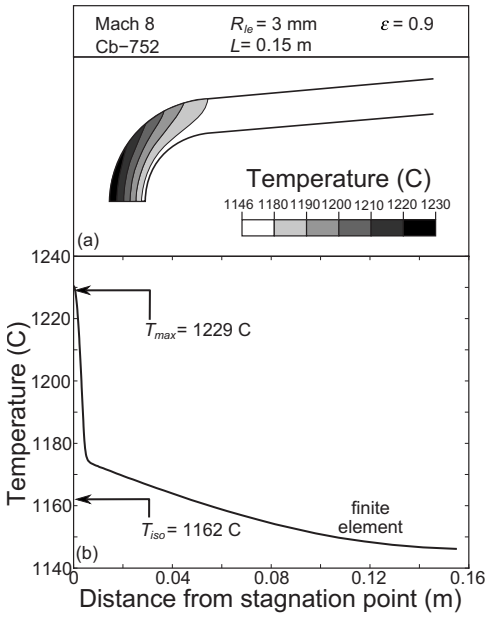

Fig. 12 (*a*) Contours of the temperatures induced in the niobium alloy at Mach 8 when the heat pipe is functioning. (*b*) The temperatures along the external surface with analytic results for T_{iso} and T_{max} for ϵ=0.9 are superimposed.

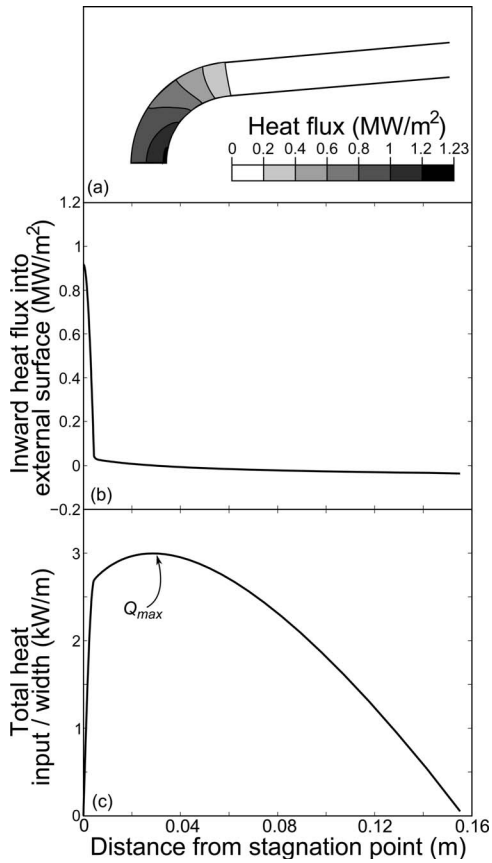

Fig. 13 Heat flows at Mach 6 for an Inconel 625 leading edge. (*a*) Contours of heat flux at the design length $L=0.15$ m and $\epsilon=0.9$. (*b*) Local heat flux into the exterior surface. (*c*) Integrated heat input from the leading edge. At the design length the net total heat input is zero.

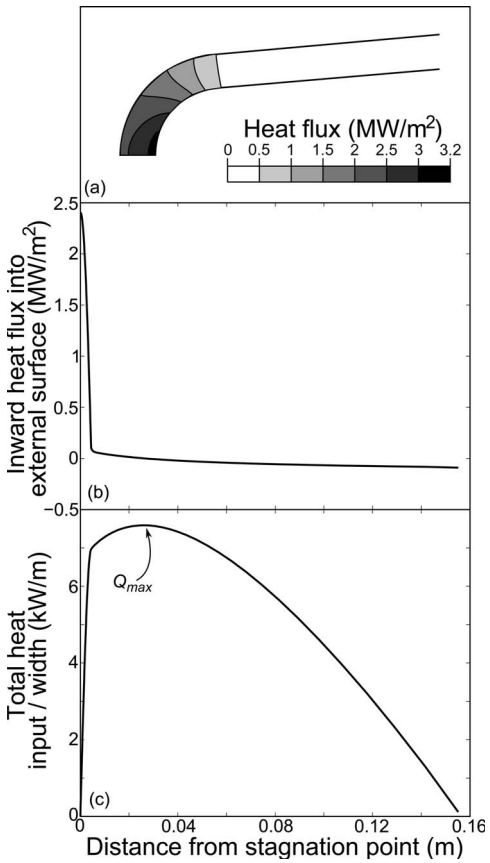

Fig. 14 Heat flows at Mach 8 for a Cb-752 leading edge. (*a*) Contours of heat flux at the design length $L=0.15$ m and $\epsilon=0.9$. (*b*) Local heat flux into the exterior surface. (*c*) Integrated heat input from the leading edge. At the design length the net total heat input is zero.

stagnation plane. Temperatures defined in this manner are compared with the analytic estimates on the figures. The close correspondence demonstrates the utility of the analytical approach for initial design purposes. Moreover, temperature comparisons along the flat section affirm that T_{iso} is independent of the material choice. Recalling that T_{iso} dictates the choice of the working fluid, then for a 3 mm radius, at Mach 6, either sodium or potassium should be applicable, while at Mach 8, lithium would be preferred, as elaborated later.

The corresponding heat fluxes are summarized in Figs. 13 and 14. Those at the external surface are directed inward over the curved section but outward over most of the flat segment. Consequently, the cumulative heat input reaches a maximum just beyond the transition and declines thereafter; by definition, the net heat input is zero at the design length. The maxima are the most pertinent since these are the fluxes that must be redistributed by the working fluid in the heat pipe. These are $Q_{max}=3$ kW/m at Mach 6 and $Q_{max}=7.6$ kW/m at Mach 8, with approximate scaling, $Q_{max}\sim u_\infty^3$. The contours over the curved region affirm that the flux entering the heat pipe near the stagnation plane is largest: $\dot{q}_{max}\approx 1.2$ MW/m^2 at Mach 6 and $\dot{q}_{max}\approx 3.2$ MW/m^2 at Mach 8. (Note that these are significantly lower than the cold-wall fluxes typically cited for leading edges at the same Mach number, altitude and radius.)

Mises stresses. Contours of the Mises stresses are plotted in Fig. 15. The maxima at the tip are about 10% larger than the analytic estimates (Fig. 8). The difference is attributed to a small bending effect not accounted for in the analytic formula. The results for Inconel 625 (Fig. 15(*a*)) reveal that, even at Mach 6, the stresses approach the yield strength at the associated temperature (see Fig. 3). Indeed, the most failure susceptible element at the tip on the exterior surface is sufficiently close to yield that the safety margin would be unacceptable. The corresponding Mises stress contours for the niobium alloy (Fig. 15(*b*)) reveal much larger margins of safety, even at Mach 8. The niobium alloy is preferable because of its higher conductivity, lower modulus, and lower thermal expansion, all of which decrease the maximum stress.

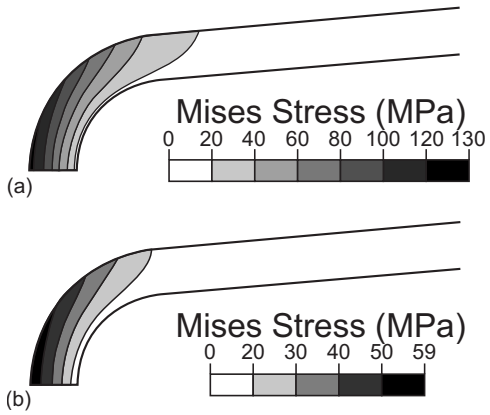

Fig. 15 Mises stress contours when the heat pipe is functioning: (*a*) Mises stresses for Mach 6 with nickel-based superalloy Inconel 625; and (*b*) Mises stresses for Mach 8 with niobium alloy Cb-752

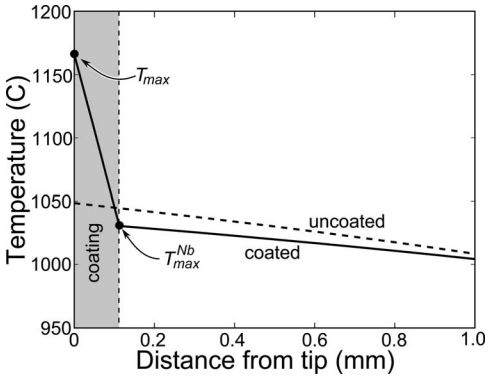

Fig. 16 The temperature distribution through a niobium leading edge with a 100 μm anti-oxidation environmental barrier coating for a Mach 7 vehicle

Coupled with greater yield strength at higher temperatures, niobium alloys are clearly a superior design choice.

4 Influence of Coatings and Transients

Coatings. The nickel and niobium alloys to be used may require oxidation protection coatings to assure multiflight capability. This is especially true for the Nb alloys being contemplated for use at the higher Mach numbers. To examine the possible effect of these coatings on temperatures in the system, a numerical calculation has been conducted for a Mach 7 design using a Cb-752 alloy with an oxidation protection coating having thickness $t_{coat}=100$ μm. The coating is considered to be highly insulating, with thermal conductivity, $k=1$ W/m K. The temperature results are summarized in Fig. 16. Note that the maximum temperature developed in the niobium has been reduced relative to that without the coating, but the coating surface becomes extremely hot. Moreover, a large temperature gradient is induced in the coating, with high likelihood of delamination [13]. The impact of coatings on the viability of the envisioned leading edge systems thus requires careful assessment that balances their benefits in environmental protection with their adverse susceptibility to spalling.

Transients. Time-dependent calculations of heat diffusion through the leading edge elucidate the transient behavior of the system at startup. The leading edge at ambient temperature is instantaneously exposed to flight conditions. To activate the heat pipe, a minimum critical temperature, T_{cr}, must be attained at the back face; subsequently it provides heat transport dependent on the ensuing back face temperature. The heat pipe is assumed to obey a heat flux law

$$\dot{q}=\left(\frac{T_{bf}-T_{cr}}{T_{iso}-T_{cr}}\right)^{m}\dot{q}_{ss} \tag{15}$$

where T_{bf} is the instantaneous temperature at the back face, $\dot{q}_{ss}$ is the heat flux at the steady state, as calculated by Eq. (13), and m is an exponent governing the rate of heat pipe startup. Once the back face reaches T_{iso}, the heat flux in the system is in equilibrium. The time-dependent thermal behavior of the Mach 7 Cb-752 system is shown in Fig. 17(*a*) for $T_{cr}/T_{iso}=0.9$ and $m=1$.

Three transient phases are evident.

Phase I. The temperature of the outer surface rises quickly. The back face temperature rises more slowly, as heat diffuses through the thickness, causing an initial rapid stress elevation (see Fig. 17(*b*)); this phase concludes with a local maximum in stress.

Phase II. The system moves toward thermal equilibrium. The Mises stress gradually declines because the temperature of the back face increases more quickly than the temperature of the front face.

Phase III. The heat pipe begins to operate. This activation dramatically slows the rise in back face temperature, as the Mises stress increases to a global maximum. These calculations suggest that the maximum stress during the transient phase does not exceed that at steady state. However, the results are highly dependent on the choice of the startup temperature and the rate exponent. Experiments and detailed modeling of the heat pipe are needed to choose these accurately.

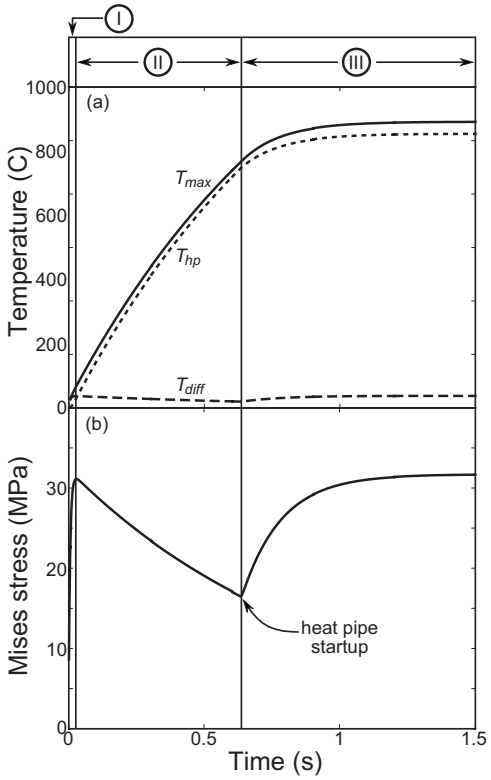

Fig. 17 The idealized behavior of the leading edge during the startup phase for a Cb-752 leading edge at Mach 7. (*a*) The temperature at the external surface T_{max}, at the back surface T_{hp}, and the difference between the two temperatures T_{diff}. (*b*) The resulting Mises stress at the stagnation point.

5 Heat Pipe Limitations

Heat pipes can fail when the heat transfer rate within the pipe is insufficient to transport the incident heat flux. Several operational phenomena affect this limit [12,14]. Only three are relevant to the leading edge environment: (i) the *sonic limit*, encountered when the mean vapor flow velocity approaches transonic values; (ii) the *capillary limit*, which arises when the drops in liquid and vapor pressures approach the capillary pumping pressure available within the wick; and (iii) the *boiling limit*, occurring when a critical superheating of the vapor is attained and bubbles stabilize in the wick of the evaporator zone. Detailed analyses of these phenomena, which relate these limits to the thermophysical properties of the working fluid, were derived for a hollow cylindrical heat pipe [12,14,15], which is not directly applicable here. For the leading edge, the corresponding analysis has been conducted for the geometry depicted in Fig. 18, and the upper portion of the leading edge is treated as a planar heat spreader. The leading edge is constructed either from Inconel 625 with thermochemically compatible sodium as the working fluid, or Cb-752 with lithium as the working fluid. The wick system is a woven wire mesh of the same material as the case.

5.1 Sonic Limit. The sonic limit is reached when the absorbed thermal flux per unit width is given by [14]

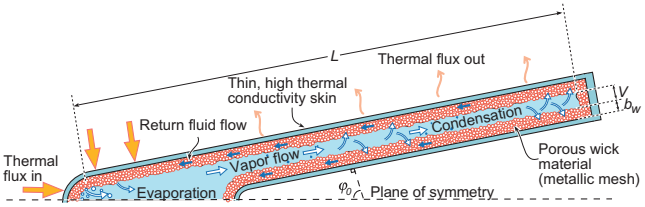

Fig. 18 A cross-sectional schematic showing the operating principles and relevant geometry of a heat plate leading edge

$$Q_{\max}^{\text{son}} = V\rho_v\lambda\left(\frac{\gamma R_g T_{\text{iso}}}{2(\gamma+1)}\right)^{1/2} \tag{16}$$

where V is the vapor space height (see Fig. 18), ρ_v is the vapor density, λ is the latent heat of vaporization of the working fluid, γ is the heat capacity ratio ($\gamma=1.67$ for monatomic sodium and lithium vapor), and R_g is the gas constant for the vapor species within the heat pipe ($R_{\text{Na}}=361$ J/kg K and $R_{\text{Li}}=120$ J/kg K). The isothermal operating temperature of the heat pipe T_{iso} (which equals the liquid-vapor saturation temperature) is limited by the onset of rapid softening and high creep rate of the case material. Note that only at low T_{iso} is the sonic limit likely to restrict the heat transport rate.

5.2 Capillary Limit. The capillary limit can be derived by a pressure balance across the length of the heat pipe

$$\Delta P_{\max}^{\text{cap}} = \Delta P_l + \Delta P_v \tag{17}$$

where $\Delta P_{\max}^{\text{cap}}$ is the maximum capillary pumping pressure, with ΔP_l and ΔP_v the liquid and vapor pressure drops, respectively. The additional pressure drops attributed to inertial effects upon evaporation and condensation of the working fluid are deemed negligible [14]. The maximum capillary pumping pressure is given by the Young–Laplace equation [12,14,15] as

$$\Delta P_{\max}^{\text{cap}} = \frac{2\sigma}{R_{\text{eff}}} \tag{18}$$

where σ is the liquid surface tension and R_{eff} is the "effective pore radius" (the radius of curvature at the liquid-vapor interface in the evaporator zone), which is a function of the porous wick geometry. Its value has been experimentally determined for numerous wick structures and porosities. The assumed effective pore radius is $R_{\text{eff}}=1.27\times10^{-4}$ m, which corresponds to a woven mesh wick with ~4 cells/mm [14].

The maximum pressure drop in the liquid within the wick can be calculated from Darcy's model of laminar flow through a porous medium

$$\Delta P_l = \frac{\eta_l Q_{\max}^{\text{cap}}}{4\kappa b_w \rho_l \lambda} L_{\text{tot}} \tag{19}$$

where η_l is the liquid dynamic viscosity, κ is the wick permeability, b_w is the wick thickness, and ρ_l is the liquid density. The woven mesh wick with four unit cells per millimeter has permeability of $\kappa=1.93\times10^{-10}$ m^2 [14]. The absence of an adiabatic section implies that the evaporator zone length L_e and the condenser zone length L_c together occupy the entirety of the heat pipe such that $L_{\text{tot}}=L_e+L_c$.

When inertial forces dominate viscous forces, and the vapor is in the incompressible, laminar flow regime, as is the case here, the maximum vapor pressure drop can be derived from the governing equations describing the velocity distribution for fully developed fluid flow in a rectangular duct

$$\Delta P_v = \frac{6\eta_v Q_{\max}^{\text{cap}}}{V^3\rho_v\lambda} L_{\text{tot}} \tag{20}$$

where η_v is the vapor dynamic viscosity.

Substituting Eqs. (18)–(20) into Eq. (17) and solving for $Q_{\max}^{\text{cap}}$ give an expression for the maximum absorbed thermal flux per unit width when constrained by capillary pumping limits

$$Q_{\max}^{\text{cap}} = \frac{4\sigma\lambda}{L_{\text{tot}}R_{\text{eff}}}\left(\frac{12\eta_n}{V^3\rho_v} + \frac{\eta_l}{2\kappa b_w\rho_l}\right)^{-1} \tag{21}$$

Liquid sodium has a heat of vaporization two orders of magnitude lower than liquid lithium at the same temperature, suggesting that the capillary limit is particularly relevant to the sodium-Inconel system.

5.3 Boiling Limit. The boiling limit is reached first where the thermal flux is largest, at the point where the stagnation line intercepts the inner surface of the heat pipe wall (see Figs. 13(*a*) and 14(*a*)). From direct application of Fourier's law, the boiling limit is given by

$$\dot{q}_{\max}^{\text{boi}} = \frac{k_w}{b_w}\Delta T_{\text{crit}} \tag{22}$$

where k_w is the thermal conductivity of the saturated wick. The critical superheat, ΔT_{crit}, is given by [14]

$$\Delta T_{\text{crit}} = \frac{2\sigma T_{\text{iso}}}{\lambda\rho_v}\left(\frac{1}{R_b} - \frac{1}{R_{\text{eff}}}\right) \tag{23}$$

where $R_b=10^{-7}$ m is an order-of-magnitude estimation of the bubble radius at nucleation. The saturated thermal conductivity for a sintered woven mesh wick is given by

$$k_w = k_l\left(\frac{k_s}{k_l}\right)^{(1-\beta)^{0.59}} \tag{24}$$

where k_l is the liquid thermal conductivity, k_s is that for the solid, and β is the wick porosity ($\beta=0.63$). The maximum heat flux at the stagnation line, $\dot{q}_{\max}$, must be less than the allowable maximum local heat flux, $\dot{q}_{\max}^{\text{boi}}$.

For the geometry under consideration, the heat flux into the heat pipe is not uniform. We define the evaporator length as $L_e = Q_{\max}/\dot{q}_{\max}$, where $\dot{q}_{\max}$ is the maximum heat flux entering the vapor from the heat pipe wall at the stagnation point (see Figs. 13(*a*) and 14(*a*)). The total heat, which can be transferred from the wall to the fluid, is conservatively given by

$$Q_{\max}^{\text{boi}} = \dot{q}_{\max}^{\text{boi}} L_e \tag{25}$$

5.4 Operational Limit Comparisons. The sonic, capillary, and boiling limits are functions of temperature-dependent thermophysical working fluid properties, namely, the liquid and vapor densities, heat of vaporization, liquid surface tension, and the liquid and vapor viscosities. Values of these properties for sodium and lithium can be found in Ref. [16], resulting in the limits for the sodium/Inconel 625 and lithium/Cb-752 systems plotted in Figs. 19 and 20. The results in Figs. 13 and 14 give L_e ~2.4 mm for both the Mach 6 and Mach 8 designs, and vapor space height $V=4.5$ mm and wick thickness of $b_w=1$ mm have been assumed. Both plots affirm that the heat pipes are functional under the proposed flight velocities and altitudes. While other limitations on the heat pipe operation exist, such as acoustic fluctuations due to aerodynamic loadings, they are currently beyond the purview of the standard models presented here.

6 Concluding Comments

This paper contains a systematic method for calculating heat fluxes, temperatures and thermal stresses in a sharp leading edge of a hypersonic vehicle which has an integrated planar heat pipe. The boundary conditions are ascertained through the use of standard expressions involving the flight velocity and altitude, the atmospheric properties, and the geometry of the vehicle. The temperatures and stresses in the leading edge are calculated using simple approximations, which are verified with finite element

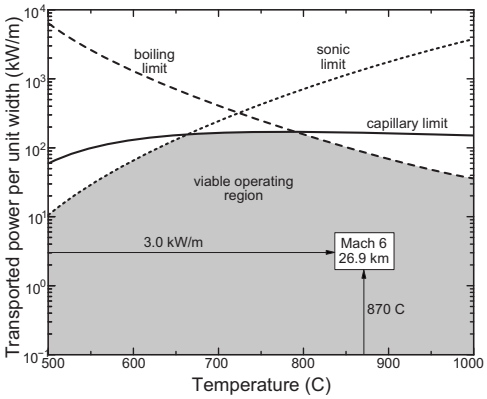

Fig. 19 The predicted operational limits of a sodium-Inconel 625 heat plate leading edge with thermal flux leading edge input corresponding to Mach 6 (26.93 km, $\dot{q}_{max} \approx 1.2$ MW/m^2)

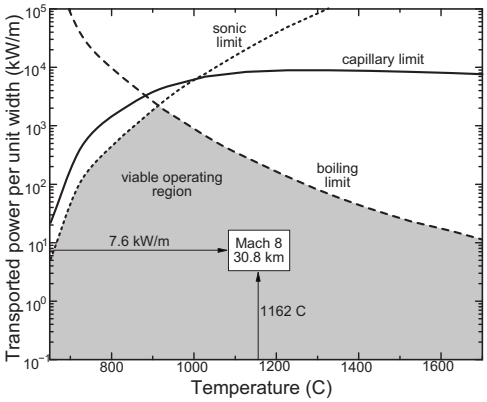

Fig. 20 The predicted operating limits of a lithium-Cb-752 heat plate leading edge with thermal flux inputs corresponding to Mach 8 (30.76 km, $\dot{q}_{max} \approx 3.2$ MW/m^2)

simulations. Conventional heat pipe estimates are then used to show the feasibility of planar metallic leading edge heat pipes. It is shown from these results that the niobium alloy Cb-752 is a better heat pipe material than the nickel alloy Inconel 625, and that a Cb-752 heat pipe with a lithium working fluid is a feasible choice for a 3 mm radius leading edge at Mach 8 or below.

The validity of the results presented here is highly dependent on choosing the correct thermal boundary conditions. The Fay–Riddell equations [8] are the most widely accepted technique for calculating leading edge heat flux, and the Sutton–Graves correlation [10] is a good approximation of these results. This paper has extrapolated from the cold-wall heat flux to determine a hot-wall heat transfer coefficient. It is believed that this is a conservative extrapolation; that is, the heat transfer coefficient should not increase with decreasing temperature gradient.

The isothermal approximation used in the analysis assumes the ideal functioning of the heat pipe. This assumption cannot be validated through the finite element simulations performed here. Instead, a full model of the internal workings of the heat pipe is required, including evaporation, condensation, and vapor and liquid transports. Such a model is beyond the scope of this paper. However, such validation can also be provided experimentally, so planar heat pipes are being built and tested in a laser facility, which delivers high heat flux to the leading edge. While these experiments cannot replicate the boundary conditions encountered during flight, the validity of the isothermal assumption and the expression for the maximum temperature can be ascertained by implementing the corresponding boundary conditions in the analytical models.

Acknowledgment

The authors would like to thank Hossein Haj-Hariri of the Department of Mechanical and Aerospace Engineering, University of Virginia; David Marshall of Teledyne Scientific; Vince Cuda of Swales Aerospace; and George Jefferson of the Air Force Research Laboratory for discussions and very helpful assistance with this work. Funding has been provided by the Office of Naval Research through the MURI program Revolutionary Materials for Hypersonic Flight (Contract No. N00014-05-1–0439).

References

[1] Glass, D. E., Camarda, C. J., Merrigan, M. A., and Sena, J. T., 1999, "Fabrication and Testing of Mo-Re Heat Pipes Embedded in Carbon/Carbon," J. Spacecr. Rockets, **36**(1), pp. 79–86.
[2] Glass, D. E., Camarda, C. J., Merrigan, M. A., Sena, J. T., and Reid, R. S., 1999, "Fabrication and Testing of a Leading-Edge-Shaped Heat Pipe," J. Spacecr. Rockets, **36**(6), pp. 921–923.
[3] Evans, A. G., Mumm, D. R., Hutchinson, J. W., Meier, G. H., and Pettit, F. S., 2001, "Mechanisms Controlling the Durability of Thermal Barrier Coatings," Prog. Mater. Sci., **46**, pp. 505–553.
[4] Heiser, W. H., and Pratt, D., 1993, *Hypersonic Airbreathing Propulsion*, American Institute of Aeronautics and Astronautics, Washington, DC.
[5] COESA, 1976, *U.S. Standard Atmosphere*, U.S. Government Printing Office, Washington, D.C.
[6] Bertin, J. J., 1994, *Hypersonic Aerothermodynamics*, American Institute of Aeronautics and Astronautics, Washington, DC.
[7] Moeckel, W. E., and Weston, K. G., 1958, "Composition and Thermodynamic Properties of Air in Chemical Equilibrium," Technical Note 4265, National Advisory Committee for Aeronautics, Lewis Flight Propulsion Laboratory, Cleveland, OH.
[8] Fay, J. A., and Riddell, F. R., 1958, "Theory of Stagnation Point Heat Transfer in Dissociated Air," J. Aeronaut. Sci., **25**(2), pp. 73–85.
[9] Lees, L., 1956, "Laminar Heat Transfer Over Blunt-Nosed Bodies at Hypersonic Flight Speeds," Jet Propul., **26**(4), pp. 259–269.
[10] Sutton, K., and Graves, R. A., 1971, "A General Stagnation-Point Convective-Heating Equation for Arbitrary Gas Mixtures," National Aeronautics and Space Administration, Langley Research Center, Technical Report No. R-376.
[11] Svehla, R. A., 1962, "Estimated Viscosities and Thermal Conductivities of Gases at High Temperatures," National Aeronautics and Space Administration, Lewis Research Center, Technical Report No. R-132.
[12] Peterson, G. P., 1994, *An Introduction to Heat Pipes: Modeling, Testing, and Applications*, Wiley, New York.
[13] Evans, A. G., and Hutchinson, J. W., 2007, "The Mechanics of Coating Delamination in Thermal Gradients," Surf. Coat. Technol., **201**(18), pp. 7905–7916.
[14] Faghri, A., 1995, *Heat Pipe Science and Technology*, Taylor & Francis, London.
[15] Chi, S. W., 1976, *Heat Pipe Theory and Practice*, Hemisphere, Washington, DC.
[16] Ohse, R. W., 1985, *Handbook of Thermodynamic and Transport Properties of Alkali Metals* (International Union of Pure and Applied Chemistry, Chemical Data Series No. 30), Blackwell Scientific, Oxford, UK.